Astronomy & Astrophysics manuscript no. W31
October 13, 2015
© ESO 2015

arXiv:1510.01922v2 [astro-ph.GA] 10 Oct 2015

Molecular gas in absorption and emission along the line of sight to W31C G10.62-0.38

H. S. Liszt[1] & M. Gerin[2]

[1] National Radio Astronomy Observatory, 520 Edgemont Road, Charlottesville, VA, USA 22903-2475
[2] LERMA, Observatoire de Paris, PSL Research University, CNRS, Sorbonne Universités, UPMC Univ. Paris 06, École normale supérieure, F-75005 Paris, France

received October 13, 2015

ABSTRACT

Context. The sightline to W31C G10.62-0.38 was extensively observed in absorption under the PRISMAS program on Herschel.
Aims. To relate absorbing material to the older view of Galactic molecules gained from CO emission.
Methods. We used the ARO 12m antenna to observe emission from the J=1-0 lines of carbon monoxide, HCO^+ and HNC and the J=2-1 line of CS toward and around the continuum peak used for absorption studies and we compare them with CH, HNC, C^+ and other absorption spectra from PRISMAS. We develop a kinematic analysis that allows a continuous description of the spectral properties and relates them to viewing geometry in the Galaxy.
Results. As for CH, HF, C^+, HCO^+ and other species observed in absorption, mm-wave emission in CO, HCO^+, HNC and CS is continuous over the full velocity range expected for material between the Sun and W31 4.95 kpc away. CO emission is much stronger than average in the Galactic molecular ring and the mean H_2 density derived from CH, 4 cm^{-3} $\lesssim$ 2<n(H_2)> $\lesssim$ 10 cm^{-3} at 4 $\lesssim$ R $\lesssim$ 6.4 kpc, is similarly elevated. The CO-H_2 conversion factor falls in a narrow range $X_{\rm CO} = 1-2\times10^{20}$ H_2 cm^{-2} (K – km s^{-1})$^{-1}$ if the emitting gas is mostly on the near side of the sub-central point, as we suggest. The brightnesses of HCO^+, HNC, and CS are comparable (0.83%, 0.51% and 1.1% respectively relative to CO) and have no variation in galactocentric radius with respect to CO. Comparison of the profile-averaged HCO^+ emission brightness and optical depth implies local densities n(H) $\approx$ 135 ± 25 cm^{-3} with most of excitation of HCO^+ from electrons. At such density, a consistent picture of the H_2-bearing gas, accounting also for the CO emission, has a volume filling factor 3% and a 5 pc clump or cloud size.

Key words. ISM: molecules ISM: abundances ISM: structure - Galay: structure

1. Introduction

The earliest perspectives on the large-scale distribution of molecules in the disk of the Milky Way were provided by cm-wave surveys of OH (Goss, 1967) and H_2CO (Whiteoak & Gardner, 1970) seen in absorption against bright H II regions in the Galactic plane. This work extended our view of molecular gas far beyond the local clouds sampled in optical absorption, but was restricted to relatively few directions at low latitude and could not provide such basic quantities as the Galactic scale height and overall radial distribution of the molecular gas, or the size and density of the host gas clouds.

Absorption line surveys were overtaken by studies of mm-wave CO emission (Scoville & Solomon, 1975; Burton & Gordon, 1978; Clemens et al., 1988; Dame et al., 2001) whose ubiquity and ease of observation allowed discovery of GMCs (giant molecular clouds) in the disk as well as the Galactic molecular ring hosting the bulk of the molecular gas. Maps of carbon monoxide emission have come to define the Galactic distribution of molecular gas.

Nonetheless, molecular emission studies are subject to their own limitations. Emission from the J=1-0 line of CO is notoriously insensitive to the gas number density (Liszt et al., 2010) and Galactic plane surveys of emission from species that are supposedly sensitive to density such as HCO^+ and HCN (Liszt, 1995; Helfer & Blitz, 1997) have beeen extremely limited. They show little or no variation with respect to CO across the Galactic disk, which is surprising given the variation of the mean molecular density. In general, emission studies are also bedeviled by confusion between dense and diffuse gas, together with uncertainty in the volume filling factor.

Turning the tables, so to speak, sub-mm studies of newly-available atomic and molecular transitions seen in absorption using the HIFI instrument on the Herschel satellite have recently provided new insights into the physical properties of molecular gas in the Galactic disk. Observations of hydride progressions (Gerin et al., 2012) like OH^+, $OH_2{}^+$ and $OH_3{}^+$ (Gerin et al., 2010a) or NH, NH_2 and NH_3 (Persson et al.,

Send offprint requests to: H. S. Liszt
Correspondence to: hliszt@nrao.edu

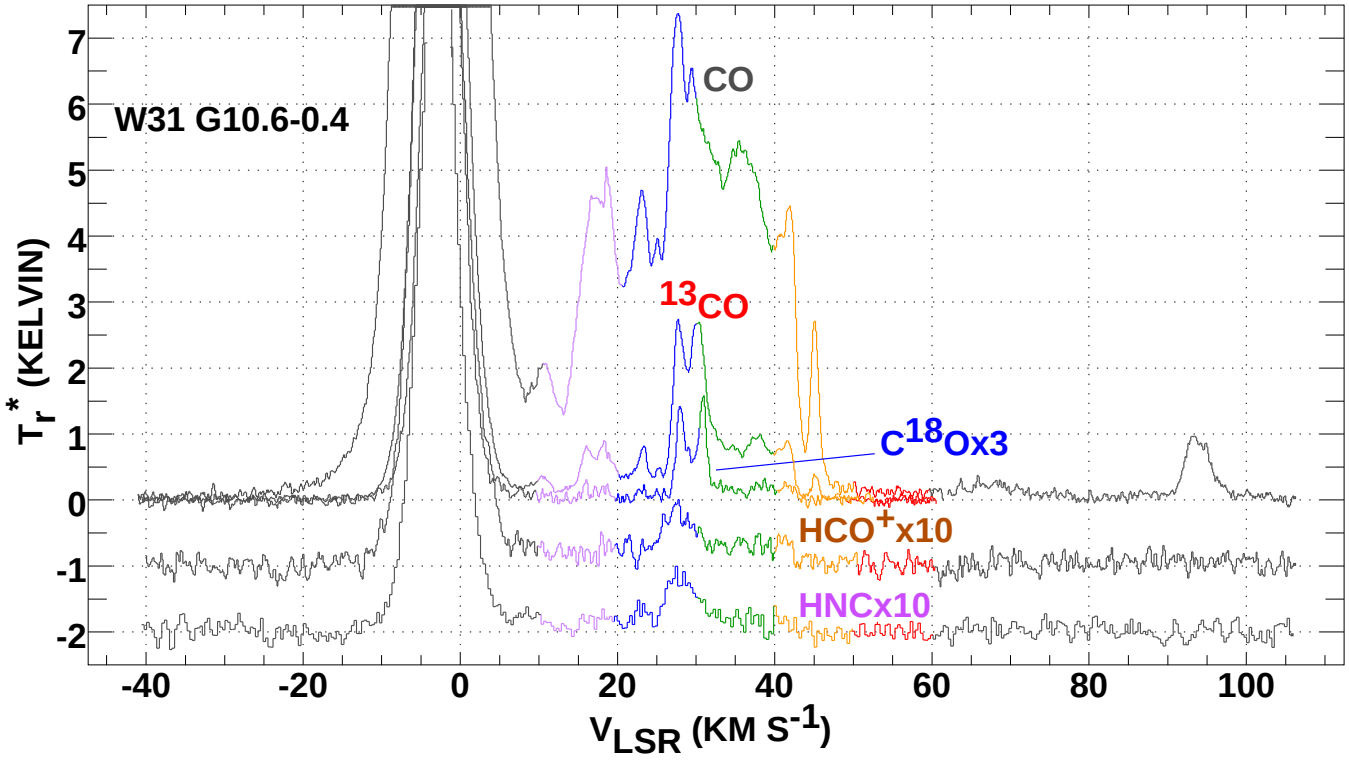

Fig. 1. Emission spectra observed at the ARO 12m telescope in 2011. The HCO^+ and HNC spectra are averages of four pointings displaced ±1.4′ to the East and North, to avoid absorption against the strongest continuum. Spectra are scaled as indicated. The spectra are color coded in 10 km s^{-1} intervals to aid in understanding of the velocity-distance transformations.

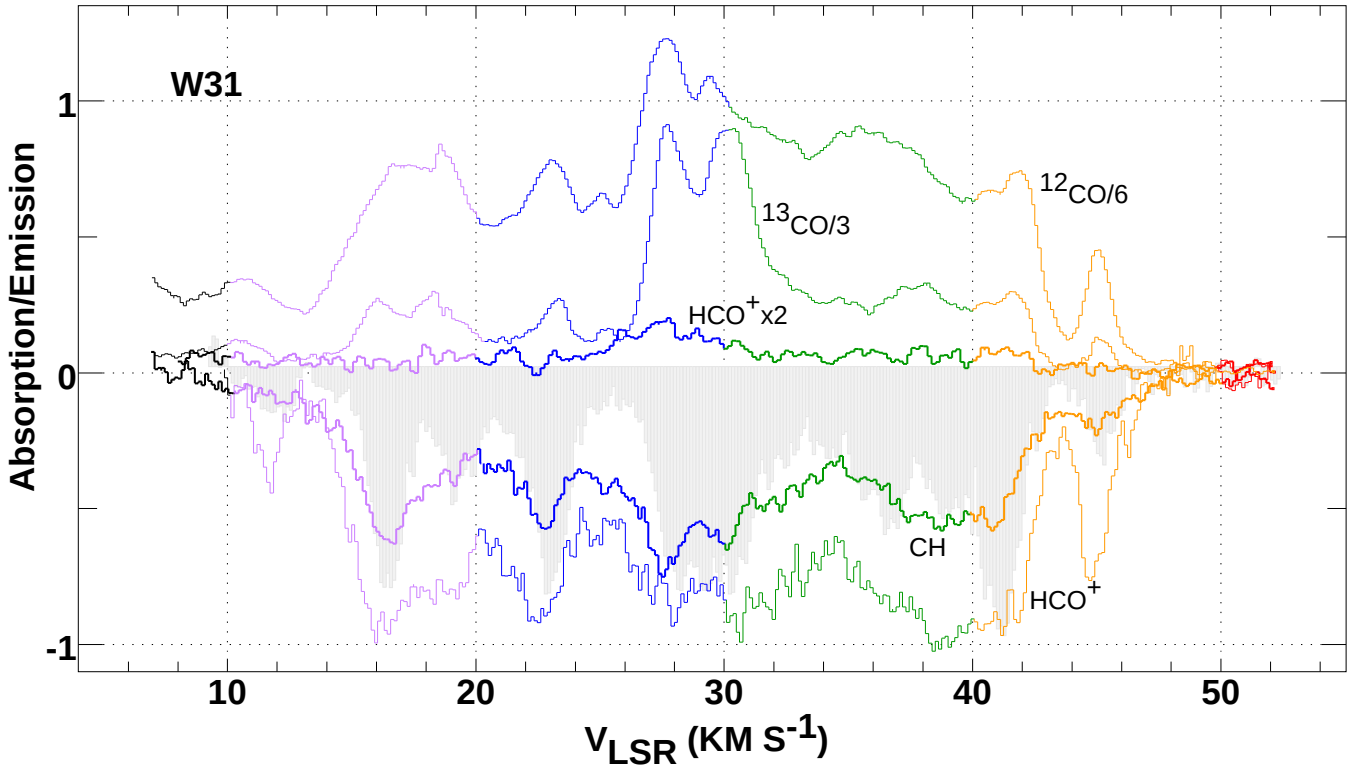

Fig. 2. Emission and absorption spectra. The color coding is as in Fig. 1. Spectra have been scaled as indicated. The CH and HCO^+ profiles are shown slightly bolder to remove some possible confusion with other spectra. The absorption spectrum of HNC is shown as a faint gray underlay.

2012) are sensitive to the presence of gas over a wide range of H_2 fraction.

Here we take a hybrid approach comparing new emission measurements at arcminute spatial resolution from the ARO 12m telescope with the wealth of absorption line data that was acquired toward W31C G10.62-0.38 in the course of the PRISMAS project on Herschel. W31C is the most strongly absorbed of all the sources in the PRISMAS sample and was explicitly targeted for its high intervening molecular column density. Along this line of sight the Sagittarius, Scutum- Centaurus and Norma spiral arms all run across the line of sight, as illustrated in Figure 6 of Sanna et al. (2014), who fixed the distance to W31C as 4.95 ± 0.5 kpc. The viewing geometry provides a high gas column density, having a high overall molecular fraction, projected onto a somewhat narrow velocity range 0 - 50 km s^{-1} because of the low Galactic longitude and relative proximity of the background target.

The plan of this work is as follows. The new and existing observational material is described in Sect. 2 and discussed in Sect. 3. In Sect. 4 we describe a formalism to interpret spectra in a manner that is appropriate to the continuous nature of the emission and absorption profiles seen toward W31C, in order to derive the variation with galactocentric radius of the CO emission, mean H_2 density and CO-H_2 conversion factor. This is done in Sect. 5 where we also derive other quantities such as the volume filling factor, cloud size and mean free path in the diffuse molecular gas. Cloud chemical abundances and Galactic gradients in the chemistry are discussed in Sect. 6 and Sect. 7 is a summary.

2. Observational material discussed here

2.1. New mm-wave emission measurements from the ARO 12m

We observed W31C G10.62-0.38 in ALMA Band 3 (86 - 116 GHz) at the ARO 12m telescope in 2011 March. We took profiles of the J=1-0 lines of ^{12}CO (CO), ^{13}CO, and C^{18}O toward the continuum peak and observed the J=1-0 lines of HCO$^+$ and HNC, and the J=2-1 line of CS, at positions displaced 1.4′ in the four cardinal directions because spectra taken toward the continuum showed clear absorption. The HCO$^+$, HNC and CS emission profiles shown here are averages of these four spectra.

All the ARO data were taken by position-switching to a reference position well above the Galactic plane, whose spectrum (showing weak CO emission near 0-velocity) was determined by position-switching against a yet more distant reference. The data were taken with an autocorrelator resolution of 97.7 kHz (velocity resolution 0.308 km s^{-1} at 100 GHz) and channel spacing of 48.8 kHz. Linear baselines were fit to emission free regions at v < −30 km s^{-1} and v > 100 km s^{-1} for the carbon monoxide lines or at v > 60 km s^{-1} for the other species.

The brightness scale of ARO 12m observations is T_r^*. At 115.3 GHz, the nominal efficiency factor needed to put such observations on the main-beam scale is (0.84 ± 0.07) [1]. However, the emission observed here is quite extended, even on 1^o scales, and no correction was applied to the observed 12m brightness. The rms noise of the spectra shown in Fig. 1 is 0.054 K for CO and 0.026 K for ^{13}CO and C^{18}O. The rms of the HNC and HCO$^+$ spectra is 0.012 K and that of CS slightly larger, 0.016 K.

We also mapped J=1-0 ^{13}CO emission on-the-fly (OTF) in a 30′ field around the continuum peak using 250 kHz filters having a velocity resolution and channel spacing 0.681 km s^{-1} at 110.2 GHz. The same reference position was used as for the pointed observations toward/around the continuum peak and the off-spectrum was added back into the cube. The typical rms in a single profile is 0.26 K.

All velocities used here are with respect to the kinematic definition of the Local Standard of Rest and labeled LSR. The high spectral resolution pointed emission profiles toward and around W31 are shown in Figs. 1, 2 and A.1. Results of the ^{13}CO OTF mapping are shown in Figs. 3 and C.1. Table 1 gives integrated intensities and ratios with respect to CO for the pointed observations shown in Fig. 1, 2 and A.1 (for CS).

Table 1. Properties of emission spectra

Species	rms K	$\int T_r^* dv$ K-km s^{-1}	$\int T_r^* dv/W_{CO}$ integrated	$\int T_r^* dv/W_{CO}$ point-point
CO	0.054	145.64(0.110)		
^{13}CO	0.028	28.39(0.066)	0.1950	0.1694(0.0805)
C^{18}O	0.024	2.82(0.054)	0.0194	0.0175(0.0275)
HCO$^+$	0.012	1.16(0.030)	0.0080	0.0082(0.0046)
HNC	0.012	0.76(0.030)	0.0052	0.0050(0.0043)
CS	0.016	1.59(0.043)	0.0109	0.0101(0.0163)

2.2. Other, existing, data

As discussed below, we used the 532 GHz CH profile of Gerin et al. (2010b) to derive the molecular hydrogen abundance assuming a value for X(CH) = N(CH)/N(H_2). This spectrum is shown in Fig. 2 with the HCO$^+$ absorption spectrum of Godard et al. (2010) and in Fig. 3 with the HNC absorption spectrum of Godard et al. (2010). (the HNC absorption spectrum is also shown in Fig. 2). The velocity resolution of the CH profile is 0.067 km s^{-1} and that for HNC is 0.26 km s^{-1}. The C II absorption profile of Gerin et al. (2015) is not shown here but is used in Fig. 6 to derive the total density n(H).

3. Observational results

New ARO emission spectra are shown in Fig. 1. Emission associated with W31 is centered just below zero velocity and extends to about +10 km s^{-1}, narrowing the range of galactocentric radius about which information may be derived. The bulk of the Galactic emission is seen at 10 - 50 km s^{-1} but a wing of weak CO emission extends to 100 km s^{-1}. A pair of narrow features is prominent in ^{13}CO and C^{18}O at v = 28 - 30 km s^{-1} and these high column density features presumably arise in the most fully molecularized material along the line of sight.

Unlike most other inner-galaxy CO profiles, the CO emission generally does not break up into discrete features attributable to clouds, separated by velocity intervals where

[1] see http://www.cv.nrao.edu/~jmangum/12meter/efficiencies.html

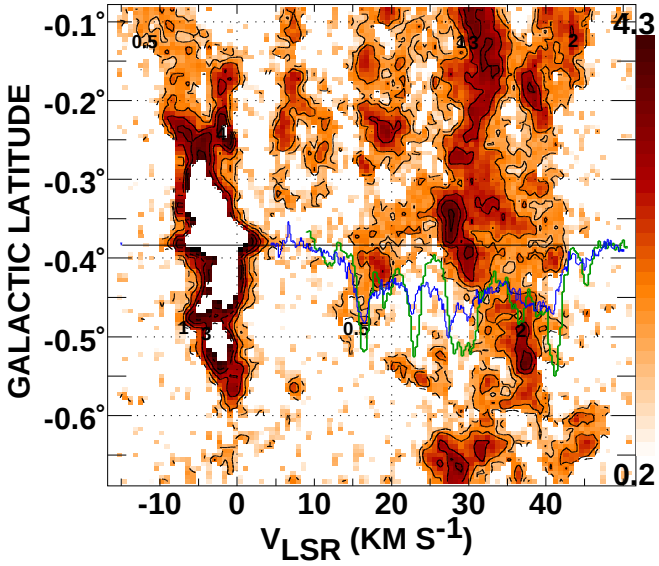

Fig. 3. Latitude-velocity diagram of ^{13}CO emission through the position of W31C G10.62-0.38 at 1′ resolution from the ARO 12m telescope. The ^{13}CO brightness scale is indicated at right, running from 0.2 to 4.3 K. The HNC absorption profile of Godard et al. (2010) is shown overlaid in green with its zero-level at the latitude of W31 and the CH absorption profile is overlaid in blue (see also Fig. 2).

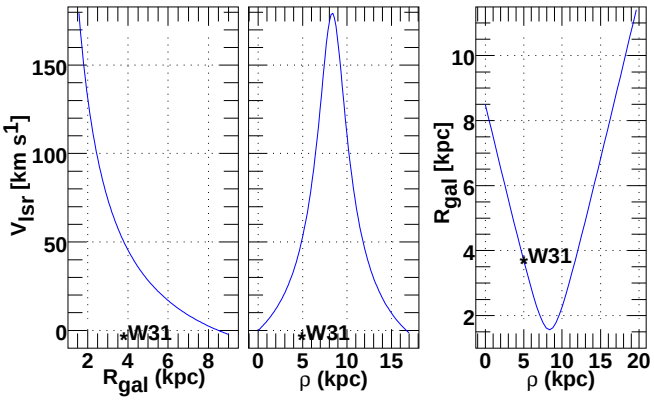

Fig. 4. Velocity and distance transformations toward W31. Left and middle: LSR velocity vs. galactocentric distance R and line of sight distance ρ for a flat rotation curve with R_0 = 8.5 kpc, Θ(R) = 220 km s^{-1}. Right: the galactocentric distance-line of sight distance relationship for R_0 = 8.5 kpc. The locus of W31 is noted in all panels, based on the 4.95 kpc distance measured by Sanna et al. (2014).

emission is weak or absent. ^{13}CO emission is also continuous over the 10 - 45 km s^{-1} range and even C^{18}O is detected over most of the interval. Profiles of HCO$^+$ and HNC emission are shown in Fig. 1 and a closeup comparison including the profile of CS J=2-1 is shown in Fig. A.1. The effective beamwidth of the profiles for HCO$^+$, HNC and CS is broadened by averaging over positions displaced 1.4′ from the continuum but the broad emission out to 42 km s^{-1} is clearly detected at all positions even in these supposedly density-sensitive species that are so much harder to excite than CO.

Fig. 2 shows a comparison of emission and absorption profiles. With the exception of the 45 km s^{-1} feature that is somewhat indistinct in CH (and much more marked in HCO$^+$), CO emission closely mirrors the absorption profiles. This is one indication that the emitting gas lies preponderantly on the near side of the Galaxy; another is that the CO emission is undetected at adjacent higher velocities just outside the kinematic span of the absorption profiles. Perhaps most importantly, no gas seen in absorption is missed in the emission profiles of CO and ^{13}CO and perhaps even in C^{18}O.

Fig. 3 shows a latitude cut through the ^{13}CO emission datacube, with the position of W31 indicated and the absorption profiles of CH and HNC superposed with their zero-levels there. The signal/noise ratio of this lower-resolution ^{13}CO dataset is substantially poorer than that of the pointed observations illustrated in Figs 1-2 (the typical rms is 0.26 K) . The narrow features at 28 - 30 km s^{-1} toward W31 are slightly separated in space but both lie in a band of widely-distributed strong emission. The spatial distribution illustrated in Fig. A1 shows that this gas lies in the outskirts of a GMC having very strong emission to the North and West.

The latitude distribution of the brightest gas in Fig. 3, at v > 25 km s^{-1}, is nearly symmetrical about the latitude of W31, suggesting that it is relatively nearby on the near side of the Galaxy. By contrast, the emission at 16 - 21 km s^{-1} is noticeably stronger nearer b = 0^o. It coincides with a local minimum in the absorption and is more likely to have a larger contribution from far-side gas.

4. Kinematic analysis of the line of sight toward W31

4.1. Galactic rotation and the velocity-galactocentric radius transformation

Previous analyses of material along individual sightlines like that toward W31 have treated line profiles using a set of velocity intervals determined by the observed spectral features. Here we develop a formalism that treats line profiles more continuously and provides an innate relationship to line of sight distance and the Galactic-scale kinematic effects that shape the profiles. The profiles and other results in the figures shown here are color-coded to provide a bridge between these two perspectives.

The basic idea behind our analysis is that the strength of observed line profiles at a given observed velocity is inversely proportional to the LSR velocity gradient at that velocity, taken with respect to line of sight distance. Multiplying an observed profile by that velocity gradient removes the distortions induced by line of sight velocity effects. The practical use of this analysis is to extend to individual profiles the same methods that are used in Galactic plane surveys to trace the variation of quantities such as the mean densities of H I or H_2 across the Galactic disk.

We define R as galactocentric radius and R_0 as the galactocentric distance of the Sun. Defining the line of sight distance

to a point at galactocentric distance R at Galactic longitude l as ρ(R) the geometry gives

$$R^2 = \rho^2 + {R_0}^2 - 2\rho R_0 \cos l \quad (1a)$$

and

$$\rho = R_0 \cos l \pm (R^2 - {R_0}^2 \sin^2 l)^{\frac{1}{2}} \quad (1b)$$

when the velocity and longitude have the same sign, R < R_0 and there are two possibilities for the kinematic distance at any given velocity, or

$$\rho = R_0 \cos l + (R^2 - {R_0}^2 \sin^2 l)^{\frac{1}{2}} \quad (1c)$$

when the velocity and longitude have opposite sign, R ≥ R_0 and there is no kinematic distance ambiguity for gas outside the solar circle.

Taking the derivative in eqn 1a,

$$\frac{dR}{d\rho} = \frac{(\rho - R_0 \cos l)}{R} \quad (2)$$

We define Θ(R) as the Galactic rotational velocity field and $\Theta_0 = \Theta(R_0)$ as the speed of Galactic rotation at the solar circle. The observed (LSR) velocity induced by Galactic rotation is

$$v(R) = R_0 \sin l * [\frac{\Theta(R)}{R} - \frac{\Theta_0}{R_0}] \quad (3)$$

so

$$\frac{dv}{dR} = -R_0 \sin l * [\frac{\Theta(R)}{R^2} - \frac{1}{R}\frac{d\Theta(R)}{dR}] \quad (4)$$

Expressing the line of sight velocity gradient as

$$\frac{dv}{d\rho} = \frac{dv}{dR}\frac{dR}{d\rho} \quad (5)$$

and assuming a flat Galactic rotation curve Θ(R) = Θ_0, combining eqns 2, 4 and 5 gives

$$\frac{dv}{d\rho} = R_0 \sin l * (R_0 \cos l - \rho) * \frac{\Theta_0}{R^3} \quad (6)$$

and inverting eqn 3 to give

$$R(v) = \Theta_0 * [\frac{v}{R_0 \sin l} + \frac{\Theta_0}{R_0}]^{-1} \quad (7)$$

provides a complete specification of the line of sight velocity gradient as a function of velocity and implied galactocentric distance within the line profile.

The basic distance-velocity relationships along the line of sight to W31C are illustrated in Fig. 4.

4.1.1. Random gas motions

Random gas motions, neglected in this explicit, analytic approach, have generally been ignored in galactic survey work because they should average out in large samples. They would act to blur and broaden the distributions in galactocentric radius that are derived here. They could be incorporated by convolving the expression for v(R) in Eqn 3 with a gaussian having the appropriate velocity dispersion and proceeding numerically.

Toward W31C the velocity gradient dv/dR varies from 5 km s^{-1} (kpc)$^{-1}$ at R = 8 kpc to 22 km s^{-1} (kpc)$^{-1}$ at R = 4 kpc with a rough mean <dv/dR> ≈ 50 km s^{-1}/4.5 kpc = 11 km s^{-1} (kpc)$^{-1}$. This can be compared with the measured one-dimensional cloud-cloud velocity dispersion of 3.0 - 4.2 km s^{-1} (Clemens, 1985; Liszt et al., 1984). The intrinsic broadening caused by random motions toward W31C is small at R = 4 kpc, and important at larger galactocentric radii near the Solar Circle.

4.2. Deriving the Galactic CO emission abundance

Surveys of Galactic CO emission compute the abundance of CO emission per kpc of path in the Galactic disk (in units of K-km s^{-1} kpc^{-1}) and plot or tabulate this quantity as a function of galactocentric radius; it is variously labelled as A_{CO} (Burton & Gordon, 1978), as here, or J_0 (Clemens et al., 1988) or called an emissivity (Pineda et al., 2013). This is done by assuming a rotation curve, and then by determining the velocities within a profile corresponding to pre-defined bins in galactocentric radius. The appropriately-integrated CO emission in the profile (units of K-km s^{-1}) and the line of sight path length in the Galactic disk are assigned to each bin and the final abundance of the survey in each bin is the summed integrated emission divide by the summed path length, as in Fig. 8 of Clemens et al. (1988) or Fig. 7 of Pineda et al. (2013). The emission abundance histogram shows the radial distribution of molecular gas over the Galaxy, and was the vehicle by which the presence of the Galactic molecular ring was first established. The confinement of molecular gas well inside the radius of the H I disk was a seminal result in ISM studies.

The analogous quantity for a single CO profile is found by computing

$$m * A_{CO}(v) = T_r^*(v) * \left|\frac{dv}{d\rho}(v)\right| \quad (8)$$

at each velocity channel, treating the velocity v= v(R) thus giving A_{CO}(R). In this expression, m = 2 if the gas is presumed to be distributed with equal liklihood at the near and far kinematic distances and m = 1 when the gas is on only one side of the sub-central point or when no kinematic distance ambiguity exists. In Galactic surveys where large numbers of sightlines are employed, m = 2 is always assumed.

4.3. Deriving the mean number density from absorption profiles

With absorption profiles the observed optical depth of species Q at velocity v is proportional to the local number density n(Q) and inversely proportional to the Galactic velocity gradient, i.e. $\tau_Q(v) \propto n(Q)/(dv/d\rho)$). Hence multiplying an optical depth spectrum $\tau_Q(v)$ by a properly scaled velocity gradient $dv/d\rho$ yields the local number density n(Q) and the conversion from

velocity to galactocentric radius R provides the Galactic perspective. As with the emission the quantity determined is

$$\mathrm{m} * \mathrm{n(Q)(v)} \propto \tau_{\mathrm{Q}}(\mathrm{v}) * \left|\frac{d\mathrm{v}}{d\rho}(\mathrm{v})\right| \quad (9)$$

with m = 2 if there is a kinematic distance ambiguity and m = 1 otherwise (as in the present case).

Here we employ this technique to derive to derive the local space-averaged [2] number density <n(H_2)> from CH absorption, using N(CH) = 3.64×10^{13} cm^{-2} $\int \tau_{\mathrm{CH}}(\mathrm{v})d\mathrm{v}$ (Gerin et al., 2010b) and N(CH)/N(H_2) = X(CH) = 3.5×10^{-8} (Sheffer et al., 2008) so that N(H_2) = $1.04\times10^{21}\int\tau_{\mathrm{CH}}(\mathrm{v})d\mathrm{v}$ cm^{-2}. We derive the mean number density of all H-nuclei density <n(H)> from the C II absorption profile using N(C^+) = 1.434×10^{17} cm^{-2} $\int\tau_{\mathrm{CII}}(\mathrm{v})d\mathrm{v}$ (Gerin et al., 2015) and the free gas phase of carbon N(C^+)/N(H) = 1.4×10^{-4} (Sofia et al., 2004; Gerin et al., 2015) so that N(H) = $1.024\times10^{21}\int\tau_{\mathrm{CII}}(\mathrm{v})d\mathrm{v}$ cm^{-2}.

The microscopic *in situ* number densities of the medium producing the observed lines differ from these space-averaged mean densities by a volume filling factor which is derived in Sect. 5 along with the *in situ* number density and other quantities..

4.4. The CO-H_2 conversion factor

The CO emission abundance A_{CO} is useful because the CO-H_2 conversion factor X_{CO} is just the ratio <n(H_2)>/A_{CO}, appropriately scaled, i.e. with X_{CO} = <n(H_2)> $\times$ (3.086×10^{21}cm)/A_{CO} given that the units of A_{CO} are K-km s^{-1} kpc^{-1}.

4.5. Galactic metallicity gradient

Our analysis depends on the abundances of the carbon-bearing species CH and (to a lesser extent) C^+ with respect to hydrogen, which we take to be constant at N(CH)/N(H_2) = 3.5×10^{-8} and N(C^+)/N(H) = 1.4×10^{-4}. Gerin et al. (2015) found no Galactic gradient in N(C^+)/N(H) when N(H_2) was derived from N(CH) but this could also be the case when the molecular fraction is high and the abundances of CH and C^+ scale in the same way with the local metallicity. The discussion is further complicated by the fact that the relevant quantities are the free gas phase abundances after depletion, whereas the Galactic gradient is measured on the metallicity itself.

In their derivation of the CO-dark H_2 gas fraction Langer et al. (2014) used an exponential Galactic carbon abundance gradient N(C^+)/N(H) $\propto$ exp(-R/6.2 kpc) following Wolfire et al. (2003), based on the [O/H] metallicity gradient at that epoch. This would imply a factor two difference between the value at R = 8.5 kpc and that at the inner edge of the Galactic molecular ring at R = 4 kpc. More recent discussions, for instance Sect. 4.3.3 of Luck & Lambert (2011), cite smaller gradients with much longer scale lengths, ranging from 12.5 kpc for [C/H] in Cepheids (Luck & Lambert, 2011) to 25 - 35 kpc for [C/H] and [O/H] in disk B-stars and H II regions (Daflon & Cunha, 2004; Maciel & Costa, 2010). Such small gradients are understandable in terms of radial mixing, see Kubryk et al. (2015) and they imply much smaller variations: For a scale length of 25 kpc, the change in metallicity over the range R = 4 - 8.5 kpc is 20%. On this basis the Galactic metallicity gradient is not included in the baseline C/H and CH/H_2 abundance ratios used in this work.

[2] i.e. at the galactocentric radius corresponding to that particular velocity

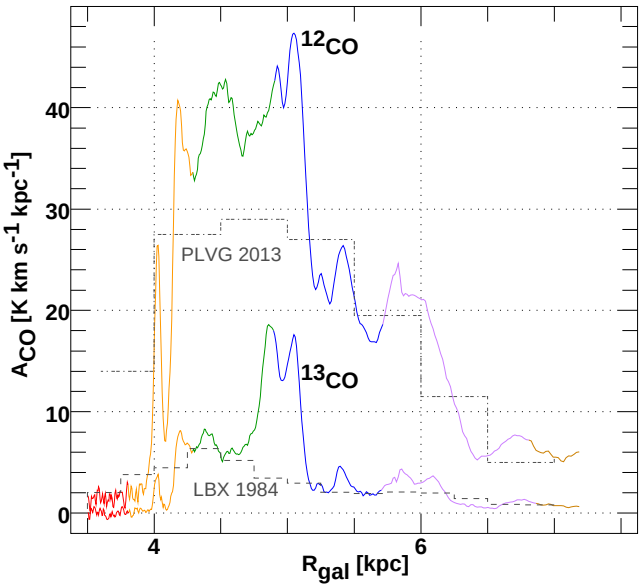

Fig. 5. Galactic abundance of CO and ^{13}CO emission vs. galactocentric distance for a flat rotation curve with R_0 = 8.5 kpc and Θ_0 = 220 km s^{-1}. The dashed histogram of the ^{13}CO abundance labelled LBX 1984 is from a re-analysis of the ^{13}CO survey data of Liszt et al. (1984) and the dashdot histogram for CO labelled PLVG 2013 was transcribed from Fig. 7 of Pineda et al. (2013). The color coding is as in previous figures.

5. Gas and cloud properties along the line of sight to W31C

Here we follow the methods outlined in Sect. 4, using the line profiles toward W31 to derive the CO emission abundance, the mean H I and H_2 densities and the quotient of the mean molecular density and CO emission abundance that is the CO-H_2 conversion factor. We derive *in situ* number densities, the typical volume filling factors of atomic and molecular gas and the size scale of clumping in the molecular gas.

5.1. The CO emission abundance

Fig. 5 shows the emission abundances for CO and ^{13}CO assuming (as in the case of blind surveys) that the gas is equally distributed at the near and far distances (m = 2 in eqn 8). Our curves in Fig. 5 would be twice higher for gas assumed to lie on only one side of the Galaxy.

Comparison with published Galactic survey results provides a valuable perspective on the line of sight to W31, but the derived quantities from older Galactic CO surveys that observed the Galaxy most widely were computed for R_0 =

10 kpc, Θ_0 = 225 km s^{-1} and have never been re-cast. They scale as $A_{CO} \propto R_0{}^{-1}$ in only the most approximate sense. Nonetheless we see from Fig. 8 of Clemens et al. (1988) a peak $J_0 * 10/8.5 \approx 30$ K-km s^{-1}kpc^{-1}, compared with 40 K-km s^{-1} kpc^{-1} in our Fig. 5.

A modern version of the CO emission abundance histogram using data in the Galactic plane is shown in Fig. 7 of Pineda et al. (2013), from which we transcribed the trace shown in Fig. 5 here. The larger-scale emission abundance histogram of Pineda et al. (2013) coincides with the results derived toward W31 for R $\gtrsim$ 5 kpc but has a somewhat smaller peak value 28 K km s^{-1} kpc^{-1} at smaller galactocentric radii.

Fig. 5 compares the abundance histogram for ^{13}CO emission toward W31 with that observed in the Galactic equator at l = 20^o - 40^o by Liszt et al. (1984), recomputed for the flat rotation curve employed here. In this case the two peaks at 28 - 30 km s^{-1} toward W31 stand out. Otherwise, the larger-scale survey results generally coincide with the result toward W31.

5.2. Locally space-averaged atomic, molecular and total densities

Fig. 6 at top shows the overall Galactic distribution of the locally space-averaged atomic and molecular mid-plane densities drawn from Pineda et al. (2013). The analogous space-averaged mean atomic and molecular densities along the line of sight to W31C after applying the analysis in Sect. 4 to the H I, CH and C II profiles are shown in the middle panel. The Galactic molecular ring structure seen in CO and C^+ emission is clearly present toward W31 but the space-averaged atomic and molecular number densities in the molecular ring toward W31 are 5-6 times higher than the Galactic average.

To derive the H I gas properties we averaged profiles from the Southern Galactic Plane Survey H I (SGPS) server [3]http://www.atnf.csiro.au/research/HI/sgps/ on either side of W31 at the same latitude and converted the emission to optical depth assuming T_K = 135 K. We then applied eqn 9 as discussed in Sect. 4.3 for the velocity interval 10 - 50 km s^{-1} with the result that N(H I) = 1.36×10^{22} cm^{-2}. The distance to W31 is 4.95 kpc (Sanna et al., 2014) and the line of sight distance to a position at R = 6.82 kpc where v = 10 km s^{-1} is 1.73 kpc, so that the mean space-averaged H I number density is 1.37 cm^{-3}. This is some three times larger than the Galactic average <n(H I)>$\approx$ 0.45 cm^{-3} shown in Fig. 6. As also shown in Fig. 6 the space averaged H I number density toward W31C varies over the range 1 cm^{-3} $\lesssim$ <n(H I)> $\lesssim$ 2 cm^{-3}.

The integrated optical depth of the CH absorption profile above 10 km s^{-1} is 18.81 km s^{-1} implying N(CH) = 3.64×10^{13} cm^{-2} $\int \tau$(CH)dv = 6.85×10^{14} cm^{-2} and N(H_2) = N(CH)/3.5×10^{-8} = 1.96×10^{22} cm^{-2}. Therefore the mean density of H-nucleii in H_2 is 2<n(H_2)> = 2 N(H_2)/3.23 kpc = 3.95 cm^{-3}. This is about two times higher than the Galactic mean at the peak of the Galactic ring in Fig. 6 but only half the peak toward W31. As shown in Fig. 6 the space averaged H_2 number density varies over the range 2 cm^{-3} $\lesssim$ 2 < n(H_2) > $\lesssim$ 12 cm^{-3}, much more widely than for n(H I).

[3]

Also shown in the middle panel of Fig. 6 is an estimate of the total hydrogen density n(H) toward W31 assuming a fixed carbon abundance N(C^+)/N(H) = 1.4×10^{-4} as discussed in Sect. 4. The overall agreement between the derived H_2 and total hydrogen distributions is proof that the high molecular densities are not artifacts of a mistaken CH abundance. However the C II line generally misses the narrow peaks in the molecular density (which are seen in CO and C I emission), suggesting that its abundance is dimininished in some portions of the absorbing material.

The integrated optical depth of the C II line above 10 km s^{-1} is 45 km s^{-1} implying N(C^+) = 6.5×10^{18} cm^{-2}, N(H) = 4.6×10^{22} and <n(H)>= 4.6 cm^{-3}. There is a 6% overall correction for the contribution of N(C I) $\approx 4 \pm 1 \times 10^{17}$ cm^{-2} (Gerin et al., 2015), i.e. N(H) = 4.9×10^{22} and <n(H)>= 4.9 cm^{-3} in total overall. N(H) derived from carbon is only very slightly smaller than the sum N(H I) + 2N(H_2) = 5.28×10^{22} cm^{-2} derived from H I and CH separately. This near-agreement implies that C II absorption does not have a substantial contribution from WIM even though WIM probably occupies nearly all of the volume toward W31C, as noted in Sect. 5.5 below. The fractional contribution of WIM toward W31C is no more than 5%, based on the detection of N II absorption Persson et al. (2014) leading to N(N^+)/N(C^+) = 1/40, i.e. some twenty times smaller than the [N]/[C] elemental abundance ratio in the gas.

5.3. The CO-H_2 conversion factor

The CO-H_2 conversion factor is computed from the ratio <n(H_2)>/A_{CO}, properly normalized and with an assumption about the near-far distribution of the CO emission on either side of the Galaxy. Fig. 6 at bottom shows the CO-H_2 conversion factor assuming that the CO emission coincides with the absorbing material on the near side of W31. Material on the near side of the Galaxy is much closer to the nominal mid-plane, typically at |z| $\approx$ 20 - 30 pc, well within one scale-height, compared to material at the far kinematic distance which would be at z| $\approx$ 80 – 100 pc. From Fig. 4 we see that material at v = 30 km s^{-1} is seen at ρ = 4 and 13 kpc , or at |z| = 28 or 91 pc, compared to a scale height for the molecular gas of 50 pc (Clemens et al., 1988). We noted in Sect. 3 that the strongest ^{13}CO emission is about symmetrically distributed in latitude with respect to W31C, and that the gas at 12-22 km s^{-1} appears more nearly confined at the equator.

The derived CO-H_2 conversion factor shown in the bottom panel of Fig. 6 has structure, but it varies far less at R = 4 - 6.5 kpc than either the molecular density or the CO abundance A_{CO} (shown as a faint trace in the lower panel of Fig. 6). The value derived here in the inner Galactic disk derived by generalizing the CH chemistry in the vicinity of the Sun, A_{CO} = $1.5 \pm 0.5 \times 10^{20}$ H_2 cm^{-2} (K km s^{-1})$^{-1}$ is comparable to the canonical value 2×10^{20} H_2 cm^{-2} (K km s^{-1})$^{-1}$ that is used in Galactic studies.

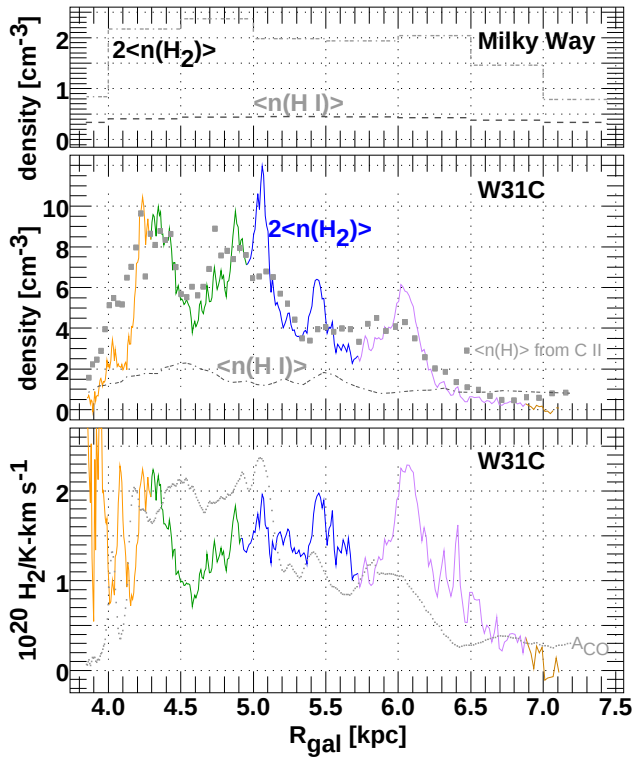

Fig. 6. Top: Milky Way space-averaged mean atomic and molecular densities from Pineda et al. (2013). Middle: mean densities 2<n(H_2)> derived from CH absorption with X(CH) = 3.5×10^{-8} shown as a solid line, color-coded as in previous figures); <n(H)> derived from C II absorption using n(C^+)/n(H) = 1.4×10^{-4} (filled light gray rectangles); and n(H I) derived from from a nearby NGPS survey H I emission profile assuming a constant spin temperature of 135 K, shown as a dashed grey line. Bottom: the CO-H_2 conversion factor derived by dividing the mean molecular density <n(H_2)> by the CO abundance A_{CO} assuming that the CO-emitting gas is on the near side . The histogram of A_{CO} is overlaid and heavily shaded with arbitrary vertical scale in the bottom panel.

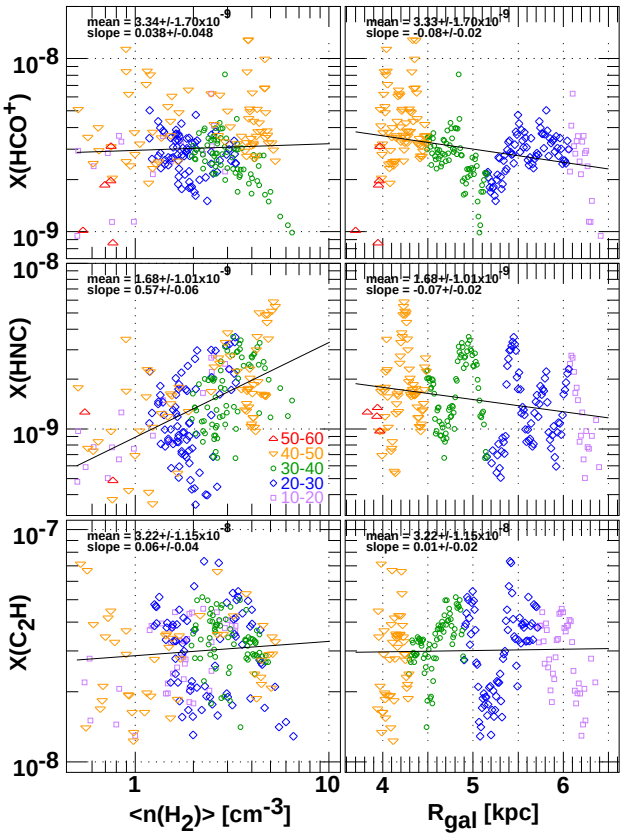

Fig. 7. Relative abundances of HCO^+, HNC and C_2H observed in absorption with respect to H_2 plotted against the local spaced-averaged mean H_2 density derived from CH (at left) and galactocentric radius (at right). Column and number densities of H_2 were derived from the CH absorption profile as discussed in Sect. 4 of the text. The mean relative abundances $\pm1\sigma$ and power-law slopes of the fitted regression lines are shown in the individual panels.

5.4. In situ number density

5.4.1. The *in situ* number density of H_2-bearing gas

The easiest and widest surveys of molecular gas in the Galactic disk are those of CO emission, which is notoriously insensitive to the density. In diffuse gas when CO is weakly-excited and far below thermalization, the excitation temperature of the J=1-0 line of CO is proportional to the thermal pressure of H_2, corrected for the line optical depth (Smith et al., 1978; Liszt & Lucas, 1998; Liszt & Pety, 2012). A similar situation arises with the fine structure lines of neutral atomic carbon (Jenkins & Tripp, 2011) from which the thermal presssure of the diffuse ISM (but not the temperature or density separately) is usually derived.

Comparison of the emission brightness and absorption optical depth of strongly-polar species such as HCO^+ can be used to derive the *in situ* number density to which emission or absorption measurements alone are notoriously insensitive. A minimum number density estimate can be derived under the assumption that the gas is diffuse, with most of the free gas phase carbon in the form of C^+ so that electrons provide most of the rotational excitation for strongly-polar species (Liszt, 2012). Because the excitation arises from electrons that are contributed by C^+ and atomic hydrogen the density so derived is the total density n(H) and is only weakly dependent on the molecular fraction. The mean brightness of the HCO^+ emission shown in Fig. 1, 0.03 K and the mean ratio of the brightness of HCO^+ to CO, 1%, are entirely typical of what is observed for diffuse cloud sightlines near the Sun (Lucas & Liszt, 1996), but observations of C^+, CH and CO toward W31 provide constraints on this interpretation, so that it need not be accepted ad hoc.

Fig. 1 of Liszt (2012) plots the predicted brightness of the J=1-0 line of HCO^+ vs dN(HCO^+)/dV (which we derive from the optical depth spectrum): Results are parametrized with the number density at a fixed electron fraction x_e = n(e)/n(H) = 1.4×10^{-4} as assumed here for the relative abundance of C^+, and with the electron abundance at n(H) = 256 cm^{-3}. For convenience, Fig. B.1 here shows dN/dV for HCO^+, HNC and HCN across their absorption spectra and indicates their means, which

for HCO^+ is < dN/dV >= 1.5×10^{12} cm^{-2} (km s^{-1})$^{-1}$. The integrated brightness of the HCO^+ emission profile shown in Fig. 1 over the velocity range from 10 to 50 km s^{-1} is 1.16 K-km s^{-1} and the mean brightness over the range $10 \le v \le 50$ km s^{-1} is 0.029 K.

From the left hand panels of Fig. 1 in Liszt (2012) we find that the mean HCO^+ brightness is reproduced at the mean column density per unit velocity if n(H) $\approx$ 160 cm^{-3} for x_e = 1.4×10^{-4}. Because it ignores other contributions to the electron fraction that causes most of the excitation of HCO^+, this is an upper limit. At this density C^+ should contribute at least 80% of the total electron abundance (Gerin et al., 2015) with most of the remainder from H^+ and a smaller contribution from He^+, implying n(H) $\approx 0.8 * 160 = 128$ cm^{-3}. However, the electron fraction contributed by C^+ decreases with density as the gas supports a higher level of cosmic-ray ionization, allowing the density to be still somewhat smaller. We estimate 110 cm^{-3} $\lesssim$ n(H) $\lesssim$ 160 cm^{-3} and use n(H) $\approx 135 \pm 25$ cm^{-3} in the discussion below as a coarse average.

5.4.2. The *in situ* number density of atomic gas

The *in situ* number densities and kinetic temperatures measured in C II by Gerin et al. (2015) toward W31 were n(H) = 40 – 45 cm^{-3} and T_K = 90 - 105 K, presumably a weighted average of the molecular component at n(H) $\approx$ 135 cm^{-3} and a less dense, somewhat warmer atomic component. The thermal pressure toward W 31 fell in a narrow range about p/k = n T_K = 4000 cm^{-3} K, implying n(H I) $\approx$ 30 cm^{-3} at the temperature T_K = 135 K that we used to derive the mean H I density in Fig. 6 from the observed 21cm emission.

5.5. H I and H_2 volume filling factors

Because the space-averaged densities <n(H I)>= 1.36 cm^{-3} and 2<n(H_2)>= 3.95 cm^{-3} are so much smaller than the *in situ* densities n(H) $\approx$ 30 cm^{-3} and n(H)$\approx$ 135 cm^{-3} in the predominantly atomic and molecular components respectively, the neutral interstellar medium along the sightline to W31 must be highly clumped, with overall line of sight average volume filling factors f_{vol}(H I) $\approx$ 1.36 cm^{-3}/30 cm^{-3} = 4.6% and $f_{vol}(H_2)$ $\approx$ 3.95 cm^{-3}/135 cm^{-3} = 3%, each varying over the range 3-7% at constant *in situ* density.

Gerin et al. (2015) found an overall Galactic median total volume filling factor f_{vol} = 2.4% based on their interpretation of C II absorption toward the wide sample of sightlines in the Galactic plane sampled in the PRISMAS project, but with much higher filling factors 6%, 13% and 8% over the velocity intervals 10-23 km s^{-1}, 23-34 km s^{-1}and 34 - 61 km s^{-1} toward W31. in overall agreement with the total filling factors derived here from other considerations.

The comparably small volume filling factors determined separately from C^+ (Gerin et al., 2015) and the combination of <n(H I)> and <n(H_2)> have several implications. That they are so much less than one implies that some 90% of volume along the line of sight to W31C must be occupied by ionized gas, either warm (WIM at 8000 K) or hot (10^6 K). That they are comparable implies that most of the C II absorption arises in neutral gas, whether cold or warm, as opposed to WIM, a conclusion that is reinforced by the near equality of the total column densities N(H) inferred separately from carbon and from the sum of H I and scaled CH as discussed in Sect. 5.2

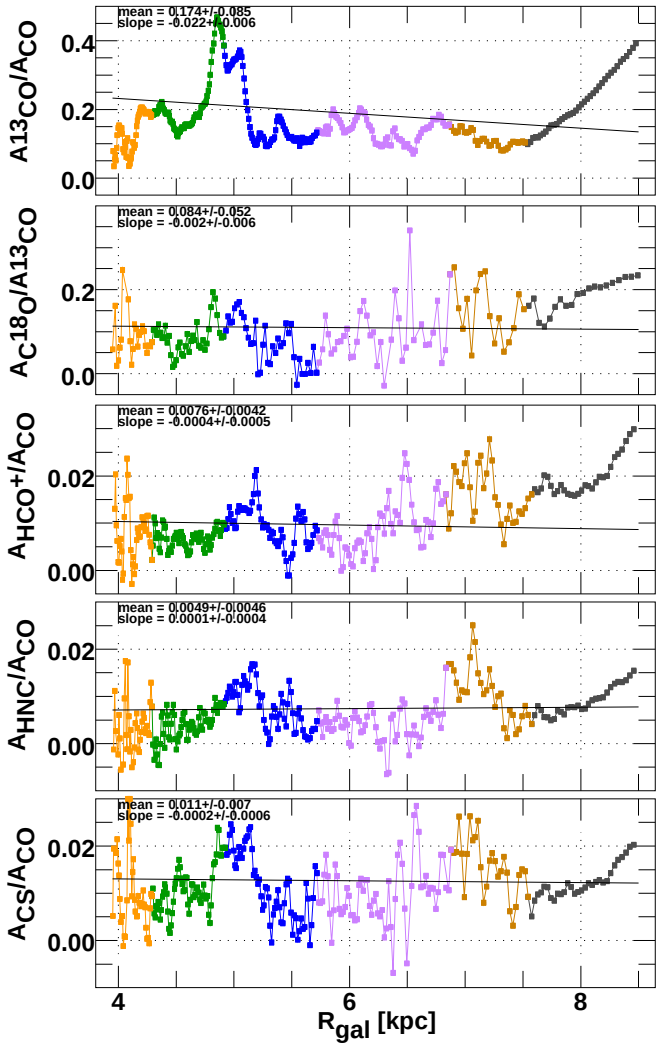

Fig. 8. Ratios of emission from ^{13}CO, HCO^+, HNC, and CS(2-1) relative to CO and $C^{18}O$ relative to ^{13}CO. The regression lines were fit to the data at R $\le$ 6.6 kpc (R $\le$ 6.3 kpc for HCO^+) to avoid contamination from the W31 complex at V $\le$ 10 km s^{-1} that appears as a false excess of emission at larger galactocentric radii for species with higher dipole moments. The mean ratios $\pm1\sigma$ and slopes of the fitted regression lines are shown in the individual panels.

5.6. A cloud size scale for clumping in the H_2-bearing gas

A size scale for cloud clumping may be derived from the continuous nature of the emission and absorption over the range v = 10 - 50 km s^{-1}. With < dN(HCO^+)/dV >= 1.5×10^{12} cm^{-2} (km s^{-1})$^{-1}$ and X(HCO^+) = 3×10^{-9} (Fig. 7 or Liszt et al. (2010)) the implied mean column density of clouds with linewidth dV (in units of km s^{-1}) is N_{cld}(H) $\approx$ 2N(H_2)

$= 10^{21}$ cm^{-2} dV [4]. For dV = 2-4 km s^{-1} these would be classic diffuse-translucent clouds with $A_V \approx$ 1-2 mag.

The number of clouds along the line of sight $\#_{clds}$ must be at least what is required to span the 40 km s^{-1} profile width, or $\#_{clds} \gtrsim$ 40 km s^{-1}/dV. The mean free path of the clouds along the 3.23 kpc path corresponding to the velocity range 10-50 km s^{-1} is then $\Lambda \lesssim 3.23$ kpc/$\#_{clds} \lesssim 0.081$ dV kpc and the typical cloud size scale D can be inferred from the derived volume filling factor $f_{vol} \approx D/\Lambda \approx 0.03$ implying D $\lesssim$ 2.7 dV pc. In turn the mean internal number density of such clouds $n_{cld}(H) = N_{cld}(H)/D \gtrsim 120$ cm^{-3}, independent of dV. Thus the parameters inferred from the HCO^+ chemistry and excitation separately yield a consistent picture of the host cloud medium. A cloud with linewidth dV = 2 km s^{-1} would have D = 5.4 pc, which at the mean line of sight distance to W31, 2.5 kpc, would subtend an angle of 7.4′ = 0.124^o, see Fig. 3.

5.7. CO, ^{13}CO and C^{18}O emission

To be sure, CO emission from the Galactic plane is not normally interpreted as arising in diffuse/translucent clouds of density n(H) $\approx$ 135 cm^{-3} so we must inquire whether the brightnesses of the carbon monoxide lines are also consistent with this interpretation. The integrated CO brightness W_{CO} = 146 K km s^{-1} at v = 10 - 50 km s^{-1} requires N(CO) $\approx 1.5 \times 10^{17}$ cm^{-2} at the typical brightness of diffuse molecular gas where 1 K km s^{-1} corresponds to N(CO) = 10^{15} cm^{-2} (Liszt, 2007). This is somewhat smaller than the column density of neutral atomic carbon N(C I) $\approx 4\pm1\times10^{17}$ cm^{-2} and very small compared to the integrated C^+ column density N(C^+) = 6.5×10^{18} derived in Sect 5.2 from the observed C II absorption line profile of Gerin et al. (2015). The main isotope CO emission is indeed compatible with the small number density derived from HCO^+.

The mean C^{18}O/^{13}CO brightness ratio, shown in Table 1 and Fig. 8, is 0.084 ± 0.052 compared to the isotopic abudance ratio 65/560 $\approx$ 0.12 near the Sun or perhaps a slightly smaller value 50/560 $\approx$ 0.09 expected in the inner galaxy (Milam et al., 2005). Thus the ^{13}CO emission nominally appears to be optically thin, despite the relatively high ^{13}CO/CO brightness ratio 0.18 ± 0.09 (Table 1 and Fig. 8) or where the ratio is as high as 0.4.

CO/^{13}CO brightness ratios as small as 5 are typically interpreted in terms of thermalized and very optically thick CO emission from dense cold molecular clouds which is inappropriate for the line of sight toward W31. Substantial fractionation of ^{13}C is expected for the gas toward W31 given that N(CO) << N(C^+) but this has never been taken into account for Galactic CO emission.

6. Cloud chemistry and and Galactic gradients

6.1. Variations of relative abundances with <n(H_2)> and R

Fig. 7 shows the relative abundances derived from the absorption spectra of HCO^+, HNC and C_2H (Godard et al., 2010), again using the CH absorption profile as a surrogate for H_2. The nearly-fixed relative abundances <X(HCO^+)>= $3.3\pm1.9\times10^{-9}$ and <X(C_2H)>= $3.2 \pm 1.2 \times 10^{-8}$ derived in this way with respect to <n(H_2)> are the same as those derived in previous absorption line work at high latitude in the Solar neighborhood (Lucas & Liszt, 2000; Liszt et al., 2010) or in the Galactic plane more generally (Gerin et al., 2011). The relative abundances of C_2H and CH are very nearly the same.

The sharper variation of X(HNC) with respect to <n(H_2)> at left in Fig. 7 with correlation coefficient r = 0.52 and power-law slope = 0.57 ± 0.06 can be interpreted as implying that regions of higher mean H_2 density, generally at smaller galactocentric radii (see Fig. 6), have a larger contribution from material having a higher mean N(H_2) per cloud, because absorption observations against compact continuum sources at high latitude near the Sun have shown that the column densities of the CN-bearing species HNC, HCN, and CN all increase abruptly when N(HCO^+) $\gtrsim 10^{12}$ cm^{-2} (Liszt & Lucas, 2001).

A variation in mean cloud column density could also be responsible for the small but statistically significant radial gradient in X(HNC) with galactocentric radius (power-law slope = -0.074 ± 0.022) seen at the right in Fig. 7: the correlation coefficient, is only r=0.22. However, the same explanation does not obviously account for the comparable Galactic gradient in X(HCO^+), (power-law slope = -0.077 ± 0.016 and correlation coefficient r=0.29) if X(HCO^+) does not vary with <n(H_2)> at left in Fig. 7.

6.2. Variations relative to CO

Table 1 gives integrated intensities and ratios with respect to W_{CO} for the pointed observations shown in Figs. 1, 2 and A.1 and Fig. 8 shows the radial variations in the ratios ^{13}CO/CO, ^{13}CO/C^{18}O, HCO^+/CO, HNC/CO and CS(2-1)/CO from the same emission spectra. Regression analysis was carried out for the channels corresponding to R < 6.6 kpc (R < 6.3 for HCO^+) at v $\gtrsim$ 10-15 km s^{-1}, so as to avoid contamination by the red wing of the emission profile from W31, whose effects are evident at larger radii.

The only statistically significant Galactic gradient in Fig. 8, amounting to a factor two across the Galactic disk, is in the ^{13}CO/CO ratio. A comparable gradient seen over the longitude range l = 20^o- 40^o was previously ascribed to a decrease in the mean column N(H) per cloud at larger radii (Liszt et al., 1984) although some role might be reserved for variation in the ^{13}C/^{12}C abundance ratio (Milam et al., 2005). A variation in mean cloud column density was already suggested from the variation of X(HNC) with <n(H_2)> in the immediately previous subsection here. The C^{18}O/^{13}CO ratio does not vary detectably, implying that optical depth effects in ^{13}CO across the Galactic disk are small, but also that a Galactic gradient in the ^{13}C/^{12}C ratio is also not an important factor in variation of the ^{13}CO/CO ratio.

No statistically significant variations with galactocentric radius are detectable in the HCO^+/CO, HNC/CO or CS(2-1)/CO ratios. This follows the pattern of previous work where such variations were undetected in wider-scale surveys along

[4] i.e. N(H_2) = (dV × dN(HCO^+)/dV)/X(HCO^+)

the Galactic equator in the inner Galaxy (Liszt, 1993, 1995; Helfer & Blitz, 1997). This general lack of variation seems surprising given the changes that are expected across the Galactic disk (Wolfire et al., 2003), the change in mean molecular density that is apparent in Fig. 6, and the implied change in the mean cloud column density that was inferred from the strong variation in the CO/^{13}CO ratio. Moreover, X(HNC) appears to increase with <n(H_2)> in Fig. 7 and <n(H_2)> is larger at smaller galactocentric radii in Fig. 6. Apparently, comparison with W_{CO} somehow compensates for other changes, perhaps in the same manner that the CO-H_2 conversion factor also does not change systematically over the inner galaxy because CO emission and CH absorption so closely resemble each other. Sakamoto et al. (1997) found a decreasing CO J=2-1/J=1-0 ratio at R > 6.5 kpc for gas lying out of the Galactic plane, but variations in the CO J=2-1/J=1-0 line ratio are not apparent for gas in the Galactic plane (Liszt, 1993; Sakamoto et al., 1997).

7. Summary

This paper is a follow-on to the PRISMAS project on Herschel, which studied emission and absorption from C^+ and absorption from a wide variety of molecular hydrides, hydride ions and heavier molecules at mm and sub-mm wavelengths toward H II regions used as background light ources in the inner galaxy. As described in Sect. 2 and 3, we presented emission profiles of the J=1-0 lines of CO, ^{13}CO, C^{18}O, HCO^+ and HNC and the J=2-1 line of CS taken at the older ARO 12m Kitt Peak antenna toward and around the Galactic HII region W31C G10.62-0.38 at 1′ resolution. Comparison of molecular emission and absorption spectra provides estimates of the *in situ* number density and volume filling factors of the host gas that can not be obtained from emission or absorption separately. From a comparison of CO emission and CH absorption we gave an independent, chemically-based derivation of the CO-H_2 conversion factor.

The sightline to W31C G10.62-0.38 at a line of sight distance ρ = 4.95 kpc is the most strongly absorbed of all those that were observed with PRISMAS in the inner Galactic disk. CH and HCO^+ absorption that best trace H_2 are continuous with relatively little contrast over the profile (see Figs. 1 and 2). ^{12}CO and HCO^+ emission profiles also show little differentiation into kinematically distinct cloud features. Even HNC, which preferentially appears in the most strongly-molecular regions, has continuous absorption and emission across the full velocity range over which ^{13}CO emission occurs (Fig. A.1).

Although the LSR velocity of W31C (-3 km s^{-1}) is anomalous given its location 4.95 from the Sun at galactocentric radius R = 3.9 kpc just inside the molecular ring, the kinematics of the intervening path are well characterized by Galactic rotation. The velocity interval over which absorption is present, up to 50 km s^{-1} corresponds to that expected from Galactic rotation. Velocity-distance transformations for the line of sight to W31C are shown in Fig. 4, based on the formalism developed in Section 4. Given the continuous and somewhat amorphous nature of the absorption and emission, we developed a method of kinematic analysis relating line profile velocity to line of sight distance ρ and galactocentric radius R via the line of sight velocity gradient for a flat Galactic rotation curve with R_0 = 8.5 kpc and Θ_0 = 225 km s^{-1}. The formalism is described in Sect. 4 where we showed how optical depth is related to locally space-averaged number density in the Galaxy (denoted here by <n(H I)>, <n(H_2)> etc) allowing a derivation of <n(H_2)> with galactocentric radius from CH absorption assuming a constant fractional abundance of CH with respect to H_2, X(CH) = N(CH)/N(H_2)= 3.5×10^{-8}. We also showed how to derive the emission abundance A_{CO} (units of K-km s^{-1} kpc^{-1}) that historically was derived statistically from large-scale CO surveys and used, for instance, to discover the Galactic molecular ring. The ratio <n(H_2)>/A_{CO}, properly scaled, is the CO-H_2 conversion factor.

The emission abundances of CO and ^{13}CO were discussed in Sect. 5.1 and shown in Fig. 5 where they are compared with previous results from Galactic surveys. The emission abundances toward W31C show the familiar Galactic molecular ring at R = 4-6 kpc, with an added contribution interior to R = 5 kpc.

In Sect. 5.2 (see Fig. 6) we characterized the sightline to W31C as having locally space-averaged atomic and molecular densities <n(H I)> $\approx 1-2$ cm^{-3} and 2<n(H_2)> $\approx 2-10$ cm^{-3} galactocentric radii 4 kpc< R < 6.5 kpc with overall means <n(H I)>= 1.36 cm^{-3} and <n(H_2)>= 3.95 cm^{-3}. These may be compared to <n(H I)>$\approx$ 0.45 cm^{-3} and 2<n(H_2)>$\approx$ 2 cm^{-3} for the galaxy at large at the same galactocentric radii. The high mean densities toward W31C presumably arise because the Sagittarius, Scutum- Centaurus and Norma spiral arms all run across the line of sight.

We derived the space-averaged H_2 density <n(H_2)> from the CH absorption profile and the relative abundance N(CH)/N(H_2) = 3.5×10^{-8} observed in the ISM near the Sun and derived the CO-H_2 conversion factor <n(H_2)>/A_{CO} = $1.5 \pm 0.5 \times 10^{20}$ H_2 (K-km s^{-1})$^{-1}$ over the inner galaxy, close to the canonical value N(H_2)/W_{CO} = 2×10^{20} H_2 (K-km s^{-1})$^{-1}$ (see Sect. 5.3 and the bottom panel in Fig 6). The CH absorption and CO emission profiles resemble each other sufficiently that the ratio <n(H_2)>/A_{CO} varies much less than either <n(H_2)> or A_{CO} alone. This supports our assumption that the CO emission arises in front of W31C, which we argued was likely to be the case given the large Galactic z-height at the far kinematic distance.

The *in situ* number density of the molecular gas was derived in Sect. 5.4.1 by comparing emission and absorption in HCO^+ and found to be modest, 2n(H_2) $\approx 135 \pm 25$ cm^{-3}. The H I column density toward W31C was derived assuming a kinetic temperature of 135 K and the *in situ* number density of the atomic gas at this temperature is n(H I) = 30 cm^{-3} at the thermal pressure p/k = 4000 cm^{-3} K derived previously from C^+ (Sect 5.4.2). The mean H I and H_2 densities bracket the density derived earlier from C II, n(H) $\approx$ 60 cm^{-3}. The CO column density N(CO) = 1.5×10^{17} cm^{-2} inferred at 2n(H_2) = 135 cm^{-3} is small compared to the column density of neutral atomic carbon N(C I) = 4×10^{17} cm^{-2} and very small compared to the total carbon column density N(C) = 7×10^{18} cm^{-2} derived from observations of the C II and C I lines.

Comparison of the space-averaged and *in situ* densities toward W31C in Sect. 5.5 translate to volume filling factors 3-7% for H I or H_2, in agreement with the overall volume filling

factors 8-13% derived earlier from C II absorption that arises ubiquitously throughout all but the very densest neutral gas. The density contrast and volume filling factor of the molecular gas imply clumping on a scale of 5.5 pc or 7′ at the mean distance to W31C as noted in Sect 5.6.

As discussed in Sect. 6.1, Fig. 7 at left shows the variation of relative abundance with <n(H_2)> for HCO^+, HNC, and C_2H representing three distinct chemical families. The relative abundances X(HCO^+) = N(HCO^+)/N(H_2) = 3.3×10^{-9} and X(C_2H) = 3.2×10^{-8} toward W31C are equal to values observed in the ISM near the Sun. Given that we used CH to infer <n(H_2)>, it follows that the HCO^+/CH and C_2H/CH ratios do not vary across the Galactic disk.

The HCO^+ and hydrocarbon relative abundances are nearly fixed in the chemistry observed near the Sun so it is probably not surprising that they show little variation with <n(H_2)> at left in Fig. 7. The increase of X(HNC) with <n(H_2)> is perhaps understandable in terms of the rapid increase of the column densities of the CN-bearing species in local diffuse clouds when N(HCO^+) $\gtrsim 10^{12}$ cm^{-2}: Regions of higher <n(H_2)> could have a larger contribution from clouds with higher column density. The decline in X(HNC) with galactocentric radius shown at right in Fig. 7 would then imply that clouds observed at larger R have smaller column density on average, which has previously been invoked to explain the gradient in ^{13}CO/CO that is shown in Fig. 8. However, the decline in X(HCO^+) with galactocentric radius is not understandable in these terms.

In Fig. 8 we showed the ratio of emission brightness of various species relative to CO across the Galactic disk and found variation only in the ^{13}CO/CO ratio, from 0.2 at R= 4 kpc to 0.1 at R = 8.5 kpc, a decline by factor two over the Galactic disk interior to the Sun as previously seen in CO surveys over the inner galaxy. As noted in Sect. 6.2, this was previously interpreted as implying that the mean cloud column density is smaller at larger galactocentric radii, consistent with the behaviour of HNC discussed in the previous paragraph.

The ratios of brightnesses HCO^+/CO, HNC/CO and CS(2-1)/CO, all $\approx$ 1%, do not vary over the inner Galactic disk in Fig. 8 and, as noted in Sect 6, this is consistent with wider but still limited surveys in the Galactic plane comparing emission from HCO^+, CS, HCN with CO and ^{13}CO. Those surveys showed that cloud features seen in ^{13}CO are also seen in the the rarer species with higher dipole moments at levels 1% - 2% that of CO. The ubiquitous emission and absorption from species other than CO toward W31C is an example of the same phenomenon.

7.1. recap

There is a very substantial legacy of absorption spectra from the Herschel mission. A relatively small investment of time spent taking complementary molecular emission spectra could be used to derive a wealth of additional information from that data.

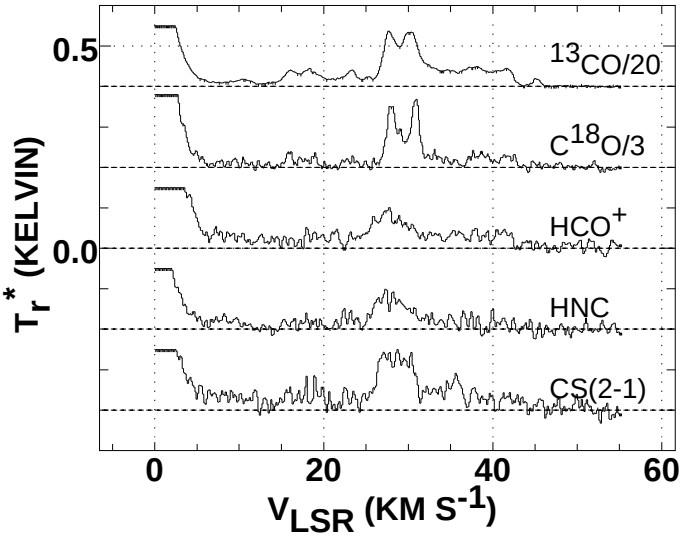

Fig. A.1. Weaker emission profiles observed at the ARO, including the HNC and CS J=2-1 lines that are not shown elsewhere in this work.

Appendix A: Emission spectra of HCO^+, HNC and CS J=2-1

Shown in Figure A.1 are the scaled emission spectra of all species except ^{12}CO, including the profile of CS J=1-1 that is not shown elsewhere in this work. A comparison of all these species with CO is shown in Fig. 8.

Appendix B: Column density spectra

Shown in Fig. B.1 are the column density spectra dN/dV of HCN, HNC and HCO^+ derived from their absorption profiles. Mean values <dN/dV> are indicated at left in the figure and used in Sect. 5.5.1 to derive the *in situ* hydrogen densities n(H_2) from a comparision of HCO^+ emission and absorption.

Acknowledgements. The National Radio Astronomy Observatory is a facility of the National Science Foundation operated under cooperative agreement by Associated Universities, Inc. The Arizona Radio Observatory is operated by Steward Observatory, University of Arizona, with partial support through the NSF University Radio Observatories program (URO: AST-1140030). We are grateful to the TAC and the Director of ARO for the opportunity to observe at the Kitt Peak 12m Telescope. This work was partly funded by grant ANR-09-BLAN-0231-01 from the French *Agence Nationale de la Recherche* as part of the SCHISM project. We thank the referee for comments that led us to clarify the text in several regards.

References

Burton, W. B. & Gordon, M. A. 1978, A&A, 63, 7
Clemens, D. P. 1985, Astroph. J., 295, 422
Clemens, D. P., Sanders, D. B., & Scoville, N. Z. 1988, Astroph. J., 327, 139
Daflon, S. & Cunha, K. 2004, Astroph. J., 617, 1115
Dame, T. M., Hartmann, D., & Thaddeus, P. 2001, Astroph. J., 547, 792

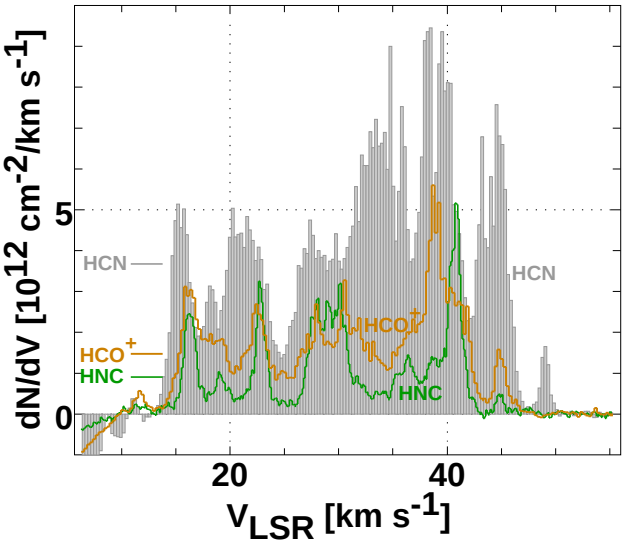

Fig. B.1. Optical depth spectra converted to column density per unit velocity. Indicated at left are the mean values at 10 km s^{-1}≤ v ≤ 50 km s^{-1}, < dN(HCN)/dV >= 3.66×10^{12} cm^{-2} (km s^{-1})$^{-1}$, < dN(HCO$^+$)/dV >= 1.48×10^{12} cm^{-2} (km s^{-1})$^{-1}$ and < dN(HNC)/dV >= 0.89×10^{12} cm^{-2} (km s^{-1})$^{-1}$

Gerin, M., de Luca, M., Black, J., Goicoechea, J. R., Herbst, E., Neufeld, D. A., Falgarone, E., Godard, B., Pearson, J. C., Lis, D. C., Phillips, T. G., Bell, T. A., Sonnentrucker, P., Boulanger, F., Cernicharo, J., Coutens, A., Dartois, E., Encrenaz, P., Giesen, T., Goldsmith, P. F., Gupta, H., Gry, C., Hennebelle, P., Hily-Blant, P., Joblin, C., Kazmierczak, M., Kolos, R., Krelowski, J., Martin-Pintado, J., Monje, R., Mookerjea, B., Perault, M., Persson, C., Plume, R., Rimmer, P. B., Salez, M., Schmidt, M., Stutzki, J., Teyssier, D., Vastel, C., Yu, S., Contursi, A., Menten, K., Geballe, T., Schlemmer, S., Shipman, R., Tielens, A. G. G. M., Philipp-May, S., Cros, A., Zmuidzinas, J., Samoska, L. A., Klein, K., & Lorenzani, A. 2010a, A&A, 518, L110

Gerin, M., de Luca, M., Goicoechea, J. R., Herbst, E., Falgarone, E., Godard, B., Bell, T. A., Coutens, A., Kaźmierczak, M., Sonnentrucker, P., Black, J. H., Neufeld, D. A., Phillips, T. G., Pearson, J., Rimmer, P. B., Hassel, G., Lis, D. C., Vastel, C., Boulanger, F., Cernicharo, J., Dartois, E., Encrenaz, P., Giesen, T., Goldsmith, P. F., Gupta, H., Gry, C., Hennebelle, P., Hily-Blant, P., Joblin, C., Kołos, R., Krełowski, J., Martín-Pintado, J., Monje, R., Mookerjea, B., Perault, M., Persson, C., Plume, R., Salez, M., Schmidt, M., Stutzki, J., Teyssier, D., Yu, S., Contursi, A., Menten, K., Geballe, T. R., Schlemmer, S., Morris, P., Hatch, W. A., Imram, M., Ward, J. S., Caux, E., Güsten, R., Klein, T., Roelfsema, P., Dieleman, P., Schieder, R., Honingh, N., & Zmuidzinas, J. 2010b, A&A, 521, L16

Gerin, M., Kaźmierczak, M., Jastrzebska, M., Falgarone, E., Hily-Blant, P., Godard, B., & de Luca, M. 2011, A&A, 525, A116

Gerin, M., Levrier, F., Falgarone, E., Godard, B., Hennebelle, P., Le Petit, F., De Luca, M., Neufeld, D., Sonnentrucker, P., Goldsmith, P., Flagey, N., Lis, D. C., Persson, C. M., Black, J. H., Goicoechea, J. R., & Menten, K. M. 2012, Royal Society of London Philosophical Transactions Series A, 370, 5174

Gerin, M., Ruaud, M., Goicoechea, J. R., Gusdorf, A., Godard, B., de Luca, M., Falgarone, E., Goldsmith, P., Lis, D. C., Menten, K. M., Neufeld, D., Phillips, T. G., & Liszt, H. 2015, A&A, 573, A30

Godard, B., Falgarone, E., Gerin, M., Hily-Blant, P., & de Luca, M. 2010, A&A, 520, A20

Goss, W. M. 1967, Astron. J., 72, 300

Helfer, T. T. & Blitz, L. 1997, Astroph. J., 478, 233

Jenkins, E. B. & Tripp, T. M. 2011, Astroph. J., 734, 65

Kubryk, M., Prantzos, N., & Athanassoula, E. 2015, Astrophysics, 580, A127

Langer, W. D., Velusamy, T., Pineda, J. L., Willacy, K., & Goldsmith, P. F. 2014, A&A, 561, A122

Liszt, H. & Lucas, R. 2001, A&A, 370, 576

Liszt, H. S. 1993, Astroph. J., 411, 720

—. 1995, Astroph. J., 442, 163

—. 2007, A&A, 476, 291

—. 2012, A&A, 538, A27

Liszt, H. S., Burton, W. B., & Xiang, D.-L. 1984, A&A, 140, 303

Liszt, H. S. & Lucas, R. 1998, A&A, 339, 561

Liszt, H. S. & Pety, J. 2012, A&A, 541, A58

Liszt, H. S., Pety, J., & Lucas, R. 2010, A&A, 518, A45+

Lucas, R. & Liszt, H. S. 1996, A&A, 307, 237

—. 2000, A&A, 358, 1069

Luck, R. E. & Lambert, D. L. 2011, Astron. J., 142, 136

Maciel, W. J. & Costa, R. D. D. 2010, in IAU Symposium, Vol. 265, IAU Symposium, ed. K. Cunha, M. Spite, & B. Barbuy, 317–324

Milam, S. N., Savage, C., Brewster, M. A., Ziurys, L. M., & Wyckoff, S. 2005, Astroph. J., 634, 1126

Persson, C. M., De Luca, M., Mookerjea, B., Olofsson, A. O. H., Black, J. H., Gerin, M., Herbst, E., Bell, T. A., Coutens, A., Godard, B., Goicoechea, J. R., Hassel, G. E., Hily-Blant, P., Menten, K. M., Müller, H. S. P., Pearson, J. C., & Yu, S. 2012, A&A, 543, A145

Persson, C. M., Gerin, M., Mookerjea, B., Black, J. H., Olberg, M., Goicoechea, J. R., Hassel, G. E., Falgarone, E., Levrier, F., Menten, K. M., & Pety, J. 2014, A&A, 568, A37

Pineda, J. L., Langer, W. D., Velusamy, T., & Goldsmith, P. F. 2013, A&A, 554, A103

Sakamoto, S., Hasegawa, T., Handa, T., Hayashi, M., & Oka, T. 1997, Astroph. J., 486, 276

Sanna, A., Reid, M. J., Menten, K. M., Dame, T. M., Zhang, B., Sato, M., Brunthaler, A., Moscadelli, L., & Immer, K. 2014, Astroph. J., 781, 108

Scoville, N. Z. & Solomon, P. M. 1975, ApJ, 199, L105

Sheffer, Y., Rogers, M., Federman, S. R., Abel, N. P., Gredel, R., Lambert, D. L., & Shaw, G. 2008, Astroph. J., 687, 1075

Smith, A. M., Stecher, T. P., & Krishna Swamy, K. S. 1978, Astroph. J., 220, 138

Sofia, U. J., Lauroesch, J. T., Meyer, D. M., & Cartledge, S. I. B. 2004, Astroph. J., 605, 272

Whiteoak, J. B. & Gardner, F. F. 1970, Astrophys. Lett, 5, 5

Wolfire, M. G., McKee, C. F., Hollenbach, D., & Tielens, A. G. G. M. 2003, Astroph. J., 587, 278

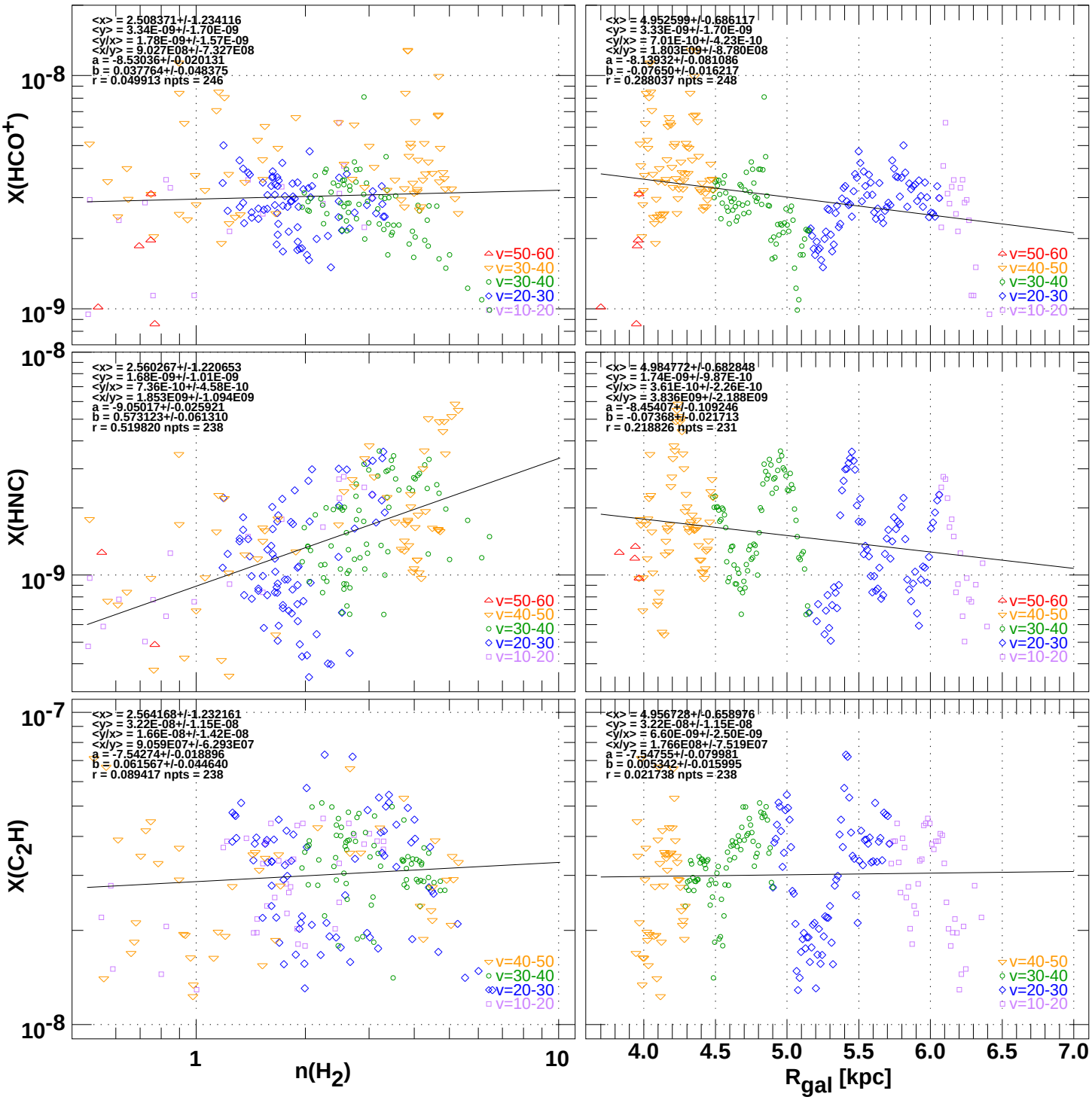
<x> = 2.508371+/-1.234116
<y> = 3.34E-09+/-1.70E-09
<y/x> = 1.78E-09+/-1.57E-09
<x/y> = 9.027E08+/-7.327E08
a = -8.53036+/-0.020131
b = 0.037764+/-0.048375
r = 0.049913 npts = 246
v=50-60
v=30-40
v=30-40
v=20-30
v=10-20
<x> = 4.952599+/-0.686117
<y> = 3.33E-09+/-1.70E-09
<y/x> = 7.01E-10+/-4.23E-10
<x/y> = 1.803E09+/-8.780E08
a = -8.13932+/-0.081086
b = -0.07650+/-0.016217
r = 0.288037 npts = 248
v=50-60
v=40-50
v=30-40
v=20-30
v=10-20
X(HCO+)
10-8
10-9
<x> = 2.560267+/-1.220653
<y> = 1.68E-09+/-1.01E-09
<y/x> = 7.36E-10+/-4.58E-10
<x/y> = 1.853E09+/-1.094E09
a = -9.05017+/-0.025921
b = 0.573123+/-0.061310
r = 0.519820 npts = 238
v=50-60
v=40-50
v=30-40
v=20-30
v=10-20
<x> = 4.984772+/-0.682848
<y> = 1.74E-09+/-9.87E-10
<y/x> = 3.61E-10+/-2.26E-10
<x/y> = 3.836E09+/-2.188E09
a = -8.45407+/-0.109246
b = -0.07368+/-0.021713
r = 0.218826 npts = 231
v=50-60
v=40-50
v=30-40
v=20-30
v=10-20
X(HNC)
10-8
10-9
<x> = 2.564168+/-1.232161
<y> = 3.22E-08+/-1.15E-08
<y/x> = 1.66E-08+/-1.42E-08
<x/y> = 9.059E07+/-6.293E07
a = -7.54274+/-0.018896
b = 0.061567+/-0.044640
r = 0.089417 npts = 238
v=40-50
v=30-40
v=20-30
v=10-20
<x> = 4.956728+/-0.658976
<y> = 3.22E-08+/-1.15E-08
<y/x> = 6.60E-09+/-2.50E-09
<x/y> = 1.766E08+/-7.519E07
a = -7.54755+/-0.079981
b = 0.005342+/-0.015995
r = 0.021738 npts = 238
v=40-50
v=30-40
v=20-30
v=10-20
X(C2H)
10-7
10-8
1
10
n(H2)
4.0
4.5
5.0
5.5
6.0
6.5
7.0
Rgal [kpc]

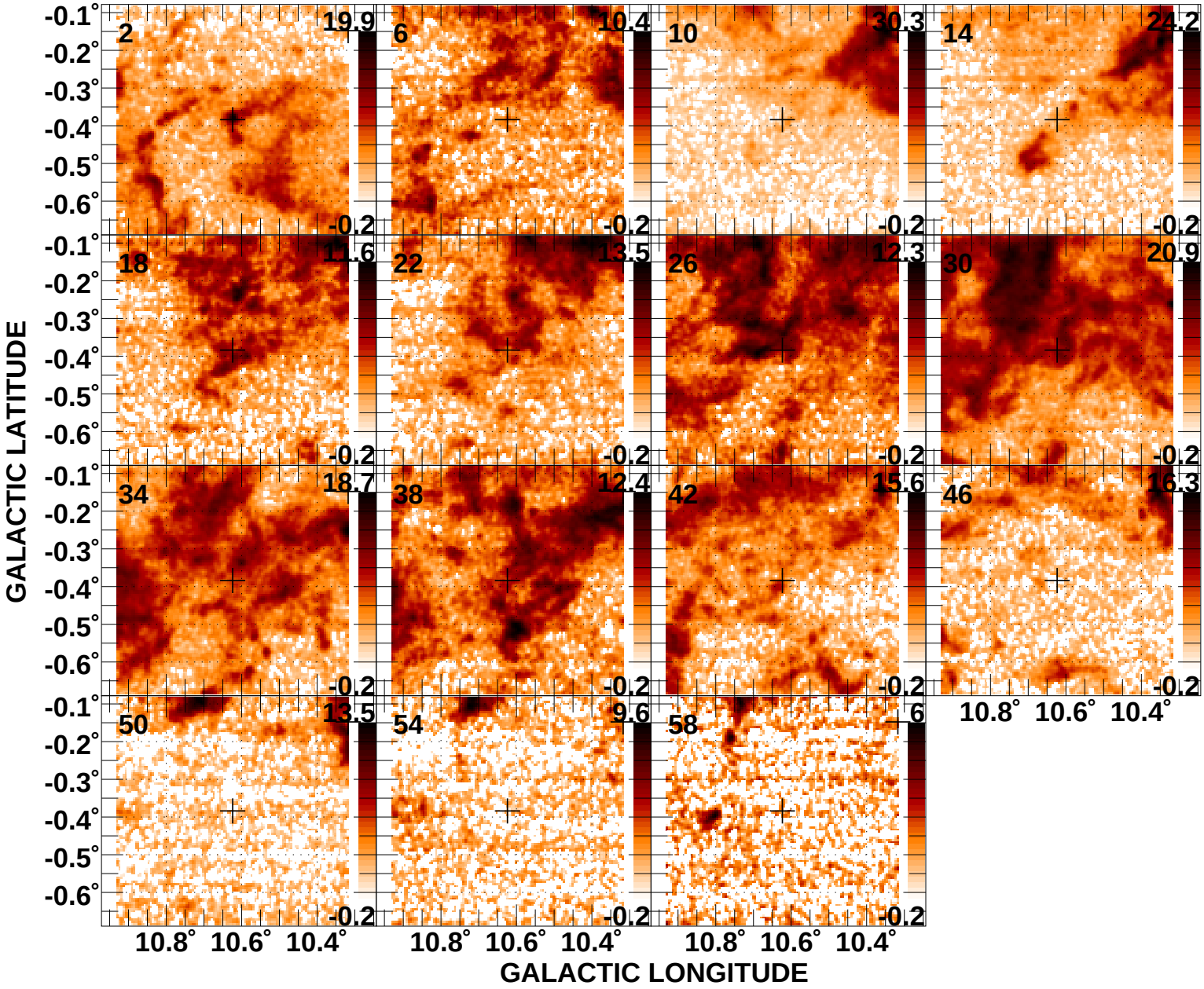
2
19.9
-0.2
6
10.4
-0.2
10
30.3
-0.2
14
24.2
-0.2
18
11.6
-0.2
22
13.5
-0.2
26
12.3
-0.2
30
20.9
-0.2
34
18.7
-0.2
38
12.4
-0.2
42
15.6
-0.2
46
16.3
-0.2
50
13.5
-0.2
54
9.6
-0.2
58
6
-0.2
-0.1°
-0.2°
-0.3°
-0.4°
-0.5°
-0.6°
10.8°
10.6°
10.4°
GALACTIC LATITUDE
GALACTIC LONGITUDE

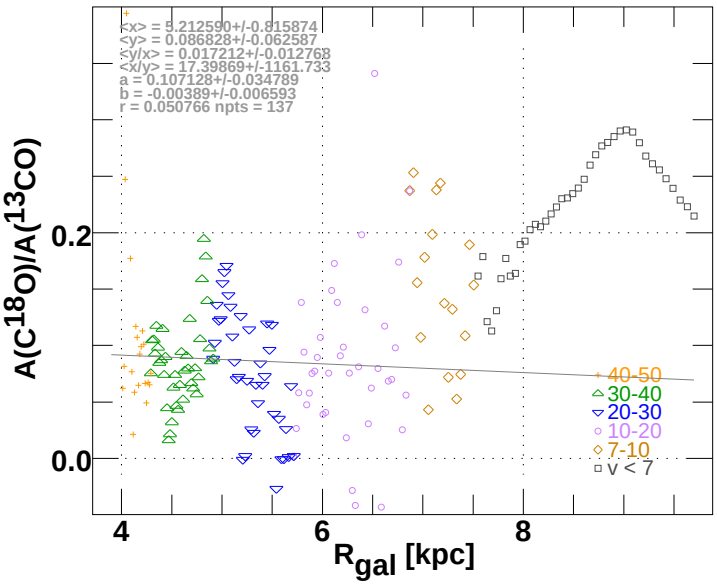
<x> = 5.212590+/-0.815874
<y> = 0.086828+/-0.062587
<y/x> = 0.017212+/-0.012768
<x/y> = 17.39869+/-1161.733
a = 0.107128+/-0.034789
b = -0.00389+/-0.006593
r = 0.050766 npts = 137
A(C18O)/A(13CO)
0.2
0.0
4
6
8
Rgal [kpc]
40-50
30-40
20-30
10-20
7-10
v < 7

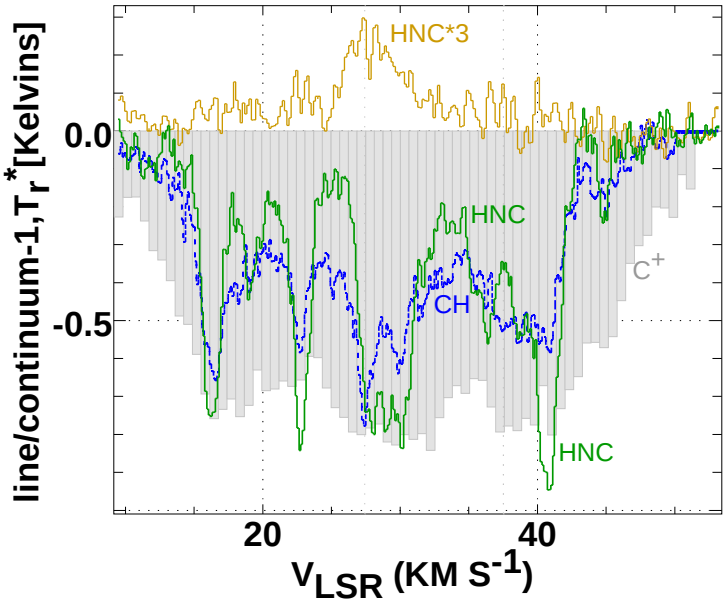
HNC*3
0.0
-0.5
HNC
CH
C+
HNC
20
40
line/continuum-1,T*r [Kelvins]
VLSR (KM S-1)